IJMMM International Journal of Minerals, Metallurgy and Materials 矿物冶金与材料学报（英文版）

$Co_{0.5}Zn_{0.5}Fe_2O_4$ modified residual carbon as an excellent microwave absorber

Yuanchun Zhang, Dacheng Ma, Xingzhao Zhang, Chuanlei Zhu, and Shengtao Gao

Cite this article as:
Yuanchun Zhang, Dacheng Ma, Xingzhao Zhang, Chuanlei Zhu, and Shengtao Gao, $Co_{0.5}Zn_{0.5}Fe_2O_4$ modified residual carbon as an excellent microwave absorber, *Int. J. Miner. Metall. Mater.*, 32(2025), No. 3, pp. 534-545. https://doi.org/10.1007/s12613-024-3028-z

View the article online at SpringerLink or IJMMM Webpage.

INTERNATIONAL JOURNAL OF
Minerals, Metallurgy and Materials

Volume 32, Number 3, March 2025
Page 534

Research Article https://doi.org/10.1007/s12613-024-3028-z

$Co_{0.5}Zn_{0.5}Fe_2O_4$ modified residual carbon as an excellent microwave absorber

Yuanchun Zhang[1,2], *Dacheng Ma*[1], *Xingzhao Zhang*[1], *Chuanlei Zhu*[1], *and Shengtao Gao*[1,2]✉

1) School of Chemical and Blasting Engineering, Anhui University of Science and Technology, Huainan 232001, China
2) Joint National-Local Engineering Research Centre for Safe and Precise Coal Mining, Anhui University of Science and Technology, Huainan 232001, China
(Received: 20 May 2024; revised: 16 October 2024; accepted: 17 October 2024)

Abstract: Microwave absorbers have great potential for military and civil applications. Herein, $Co_{0.5}Zn_{0.5}Fe_2O_4$/residual carbon (CZFO/RC) composites have been successfully prepared using a hydrothermal method. RC was derived from coal gasification fine slag (CGFS) via pickling, which removes inorganic compounds. Multiple test means have been used to study the chemical composition, crystal structure, and micromorphology of the CZFO/RC composites, as well as their electromagnetic parameters and microwave absorption (MA) properties. The CZFO/RC composites exhibit excellent MA performance owing to their dielectric and magnetic losses. When the thickness of CZFO/RC-2 ($FeCl_3·6H_2O$ of 0.007 mol, $ZnCl_2$ of 0.00175 mol, and $CoCl_2·6H_2O$ of 0.00175 mol) is 1.20 mm, the minimum reflection loss (RL_{min}) is −56.24 dB, whereas at a thickness of 3.00 mm and 6.34 GHz, RL_{min} is −45.96 dB and the maximum effective absorption bandwidth is 1.83 GHz (5.53–7.36 GHz). Dielectric loss includes interface and dipole polarizations, while magnetic loss includes current and remnant magnetic loss. CZFO/RC-2 exhibits high impedance matching, allowing microwave to enter the absorber. The computer simulation technology confirms that CZFO/RC-2 considerably decreases the radar cross-section. This study can be used to promote the use of CGFS as electromagnetic wave (EMW)-absorbing materials.

Keywords: cobalt–zinc ferrite; residual carbon; microwave absorption; coal gasification fine slag; coal-based solid waste

1. Introduction

Radar is the main long-range detection method on battlefields, and is widely employed for the detection of sea, land, air, and celestial targets [1–3]. Therefore, it is essential to reduce the radar cross-section (RCS) and radar echoes through radar stealth technology [4–8]. Radar stealth technology can be further categorized into shape and material-stealth technologies [9–11]. Electromagnetic wave (EMW)-absorbing materials convert incoming radar waves into thermal energy, which is then dissipated to eliminate radar echoes [12–15]. Thus, EMW-absorbing materials have attracted considerable research attention [16–19]. Currently, radars posing military threats are conducting search, tracking, fire control, and guidance tasks and primarily operate in the S, C, X, and Ku bands (2.0–18.0 GHz) [20–21]. In addition, the rapid development of 5G technology and the wide application of microwave technology (e.g., wireless communications) in civilian applications have numerous adverse effects [22–25]. Thus, EMW-absorbing materials can be used in civilian applications to prevent electromagnetic (EM) interference [26–29]. An ideal EMW-absorbing materials should be "thin, lightweight, broad, and strong" [30–31].

In China, hundreds of millions of tons of coal gasification fine slag (CGFS) have been accumulated in storage, greatly hindering the development of the coal chemical industry [32–33]. According to previous research, CGFS is a powder with a high residual carbon (RC) content, high moisture content, and rich pore structure [34–37]. The RC consists mainly of porous irregular particles with highly developed pore structures and a few spherical particles, some of which are embedded in irregular particles. Thus, the RC structure exhibit high orderliness [38–39]. The RC from CGFS is typically formed using a high-temperature gasification process, and it has more abundant pores, a higher specific surface area, more ordered carbon crystal structure, and more active sites than those from coal coke [40–42]. Experimental studies have indicated that RC is a dielectric type of microwave absorber, and its microwave absorption (MA) mechanism is relatively simple, resulting in its thickness is too thick and the effective absorption bandwidth (EAB) is narrow [43]. The MA performance of RC does not satisfy the requirements of modern microwave absorbers. Therefore, the performance of RC as a microwave absorber needs to be optimized by introducing other substances, such as magnetic ferrites.

Spinel ferrite microwave absorbers have received considerable attention from researchers because of their excellent MA performance [44–49]. Numerous studies suggested that the MA mechanism of spinel ferrite primarily results from natural resonance loss [50]. However, the loss frequency of spinel ferrite generally falls within the MHz frequency range [51–54]. Therefore, research has been focusing on enhancing

✉ Corresponding author: Shengtao Gao E-mail: shtgao@aust.edu.cn

the magnetic loss characteristics of this material and enriching other EM loss mechanisms to further enhance its MA characteristics. $Co_{0.5}Zn_{0.5}Fe_2O_4$ (CZFO) exhibits a high saturation magnetization and strong magneto crystalline anisotropy [55–56], allowing its impedance to be controlled by reducing its complex dielectric constant, which enhances its MA performance. The minimum reflection loss (RL_{min}) value of the nano-CZFO ferrite prepared by Liu *et al*. is −11.7 dB [57]. Zhang *et al*. [58] prepared CZFO/reduced graphene oxide absorbers using a chemical co-precipitation method involving calcination at 700°C. Ma *et al*. [59] prepared Co–Zn ferrite/graphene EMW-absorbing material using a hydrothermal method. Shu *et al*. [60] prepared Co–Zn ferrite/N-doped multiwalled carbon nanotubes for MA using a hydrothermal method. It can be seen from these studies that the MA performance of Co–Zn ferrite particles of a single component is poor. Researchers have prepared EMW-absorbing materials with excellent properties through the composite of magnetic Co–Zn ferrite and dielectric carbon matrix. However, carbon substrates [61–63] such as graphene and carbon nanotubes are expensive and require complex production paths, whereas RC from CGFS is cheap and easy to obtain.

In this study, cobalt–zinc ferrite is composited with RC to enhance its magnetic and dielectric properties. The presence of numerous heterogeneous interface structures of magnetic particles with RC can generate an interfacial polarization effect, which can enhance the conversion of EMW into thermal energy [64]. Moreover, the EM parameters of the CZFO/RC composites can be adjusted by changing the proportion of magnetic CZFO particles in this RC-based composite material. This study provides a new pathway for the utilization of CGFS that can enrich the development of coal chemistry.

2. Experimental

2.1. Materials

The RC used in this work is the same as that reported in our previous work [65–66]. All the reagents used in the experiments were of analytical grade. Iron chloride hexahydrate ($FeCl_3·6H_2O$), cobalt chloride hexahydrate ($CoCl_2·6H_2O$), zinc dichloride ($ZnCl_2$), sodium acetate anhydrous (NaAc), polyethylene glycol 4000 (PEG 4000), and ethylene glycol (EG) were purchased from Sinopharm Chemical Reagent Co., Ltd., China.

2.2. Synthesis of CZFO/RC composites

CZFO/RC were synthesized using a hydrothermal technique (Fig. 1). RC (0.6 g) was dissolved in EG (40 mL) and sonicated for 30 min. Next, $FeCl_3·6H_2O$, $ZnCl_2$, and $CoCl_2·6H_2O$ were added, and the mixture was stirred for 15 min. PEG 4000 (1.0 g) and NaAc (3.6 g) were mixed with other components. The mixture was stirred for an additional 1 h. The resulting mixture was poured into a Teflon autoclave and heated at 200°C for 10 h. Finally, the sample was rinsed with deionized water and anhydrous ethanol and dried overnight at 60°C. CZFO/RC composites with different concentrations of $FeCl_3·6H_2O$, $ZnCl_2$, and $CoCl_2·6H_2O$ were labeled as CZFO/RC-1 (0.006 mol/0.0015 mol/0.0015 mol, respectively), CZFO/RC-2 (0.007 mol/0.00175 mol/0.00175 mol, respectively), and CZFO/RC-3 (0.008 mol/0.002 mol/0.002 mol, respectively).

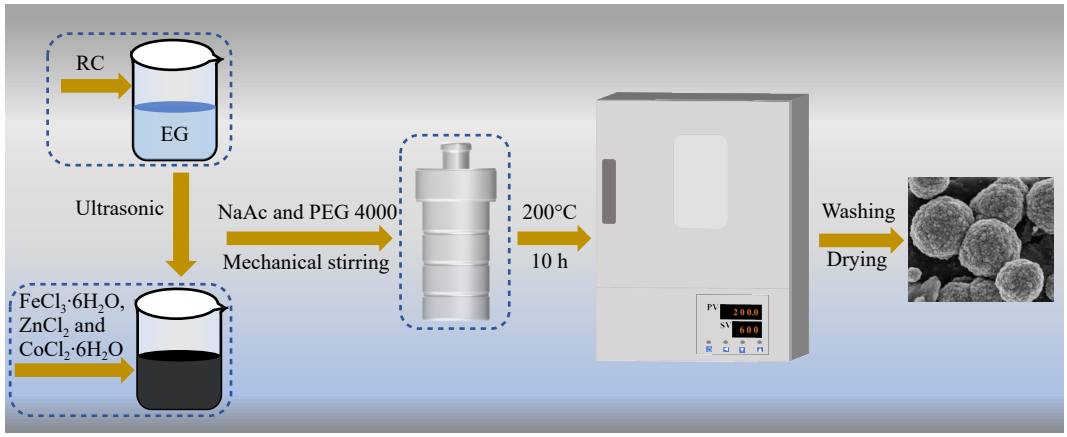

Fig. 1. Flow chart of CZFO/RC composites synthesis.

2.3. Characterization of the CZFO/RC composites

The crystal structures of the composites were tested using a LabX XRD-6000 X-ray diffractometer (Shimadzu, Japan) at scan range (2θ) of 15°–80° and scan rate of 2°/min. Fourier transform infrared spectra (FT-IR) were obtained by a VECTOR-33 device (Bruker, Germany) within the wavenumber spectrum of 500–4000 cm^{-1}. The level of graphitization of the composites was determined by Raman spectroscopy (HORIBA Jobin Yvon, France). The performance of the magnetic hysteresis loops was assessed using a PPMS-9 value stream mapping model (VSM, Quantum Design, USA) at a field intensity of ±3 T/MH. The microstructure and elemental distribution of the CZFO/RC composites were investigated via scanning electron microscopy (JEOL, Japan) and transmission electron microscopy (JEOL, Japan). X-ray photoelectron spectroscopy (XPS) was used to analyze the chemical states of C, O, Fe, Zn, and Co using an

ESCALABMK instrument (Thermo Fisher, USA). The EM parameters of CZFO/RC composites were assessed using a vector network analyzer (AV 3629D, China). This measurement was conducted in the frequency range of 2.0–18.0 GHz. A mixture of CZFO/RC composite (40wt%) and paraffin wax (60wt%) was prepared and thoroughly blended. The resulting mixture was pressed into cylindrical shapes.

3. Results and discussion

3.1. Microstructure and composition of the CZFO/RC composites

Fig. 2(a) shows the X-ray diffraction (XRD) curves of the RC and CZFO/RC. Sharp characteristic peaks occurred at 30.1°, 35.3°, 43.1°, 53.4°, 56.9°, and 62.7°, which correspond to (220), (311), (400), (422), (511), and (440) crystal faces of CZFO (JCPDS No. 22-1012), respectively. This confirms that the material contains CZFO. With an increase in the metal content in the solution, the corresponding position of the diffraction peak hardly changes, indicating the successful loading of nano-ferrite in the three synthesized samples. The high-temperature and high-pressure environment of the gasifier, to which the carbon in coal is subjected, converts some of its macromolecules into graphitized carbon through atomic rearrangement. Thus, the strong characteristic peak of graphitic carbon (002) in the three composites occurs at 25.7° [67]. With increasing nanoferrite content, the characteristic peak intensity of the (002) surface decreases, indicating that increasing the loading of nanoferrite particles on the RC surface affects the carbon peak intensity.

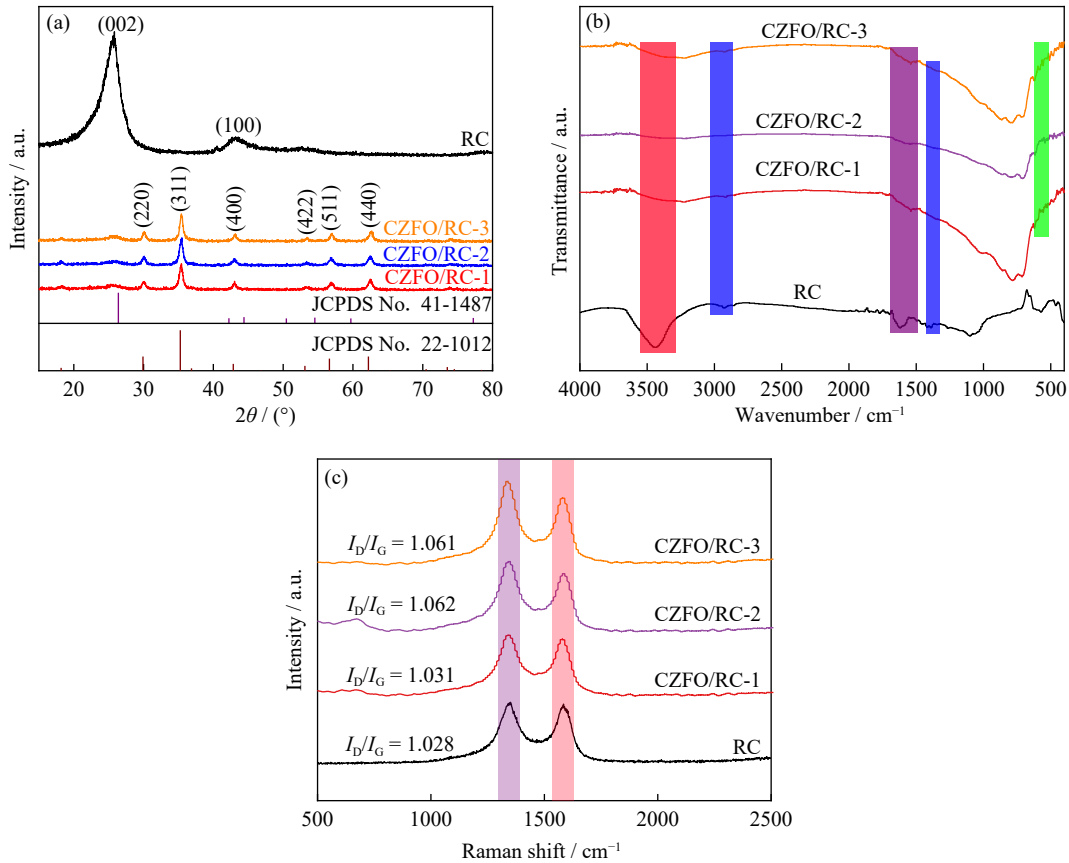

Fig. 2. XRD pattern (a), FT-IR spectra (b), and Raman pattern (c) of CZFO/RC composites and RC.

To further determine the phase structure of the CZFO/RC composites, their infrared spectra were obtained in Fig. 2(b). After loading CZFO on the RC, a large absorption peak occurs at 3200–3450 cm^{-1}, which is attributed to some residual water, the stretching vibration of hydroxy (–OH), and certain oxygen-containing groups in the RC itself. The C–H vibration can be assigned to the peak at 2940 cm^{-1}. The weak peak at 1550 cm^{-1} is attributed to C=C in CZFO/RC composite, indicating the opening of the double bond [68]. A peak at 1300 cm^{-1} was observed, which might be attributed to –OH of oxygen-containing groups in the RC. The peak corresponding to C–O stretching vibration was observed at 1048 cm^{-1}. Moreover, the peak near 1600 cm^{-1} is assigned to C=O and C–O of associated state in –COOH. The successful synthesis of ferrite is indicated by the absorption peak of the Fe–O stretching vibration at approximately 580 cm^{-1}.

Raman characterization was performed to further study the effect of the CZFO loading on the graphitization level of RC in the composite (Fig. 2(c)). The intensity ratio of D and G peaks (I_D/I_G) of CZFO/RC-1, CZFO/RC-2, and CZFO/RC-3 are 1.031, 1.062, and 1.061, respectively. Compared with pure RC, the loading of CZFO on the RC surface can considerably increase the I_D/I_G value, indicating a reduction in the RC and improvement in the electron migration ability within the composites.

VSM was employed to detect the magnetic of the CZFO/

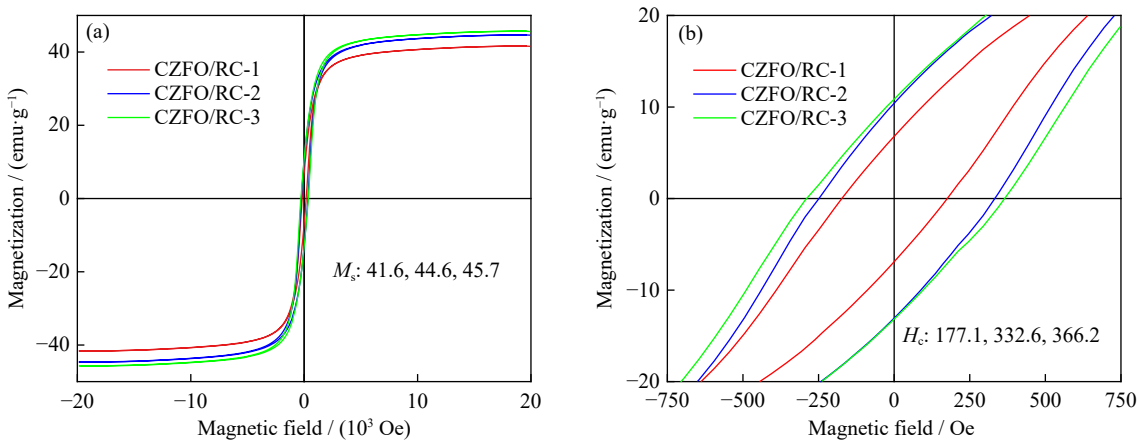

Fig. 3. (a) Hysteresis loop of CZFO/RC composites and (b) its local amplification.

RC. In Fig. 3(a), the saturation magnetization (M_s) of CZFO/RC-1, CZFO/RC-2, and CZFO/RC-3 are 41.6, 44.6, and 45.7 emu/g, respectively. Therefore, M_s is correlated with the CZFO content in the composite and increases with its increase, which also increases the EMW energy. Furthermore, in Fig. 3(b), the estimated coercivity values (H_c) are 177.1, 332.4, and 366.2 Oe, respectively. These results indicate that CZFO/RC has certain magnetic properties, which is the main reason resulting in the magnetic loss for incident EMW energy.

The scanning electron microscopy (SEM) and the transmission electron microscopy (TEM) were used to investigate morphology, microstructure, and elemental distribution of CZFO/RC composites (Figs. 4 and 5). Fig. 4(a), (d), and (g) shows that CZFO exhibits a nanospherical structure (diameter of 250–350 nm). As shown in Fig. 4(b), (e), and (h), numerous CZFO nanospheres are gathered, forming spherical shapes on the RC sheets and thoroughly combined to form multiple heterojunction interfaces. The formation of heterogeneous interfaces enhances the generation of interface po-

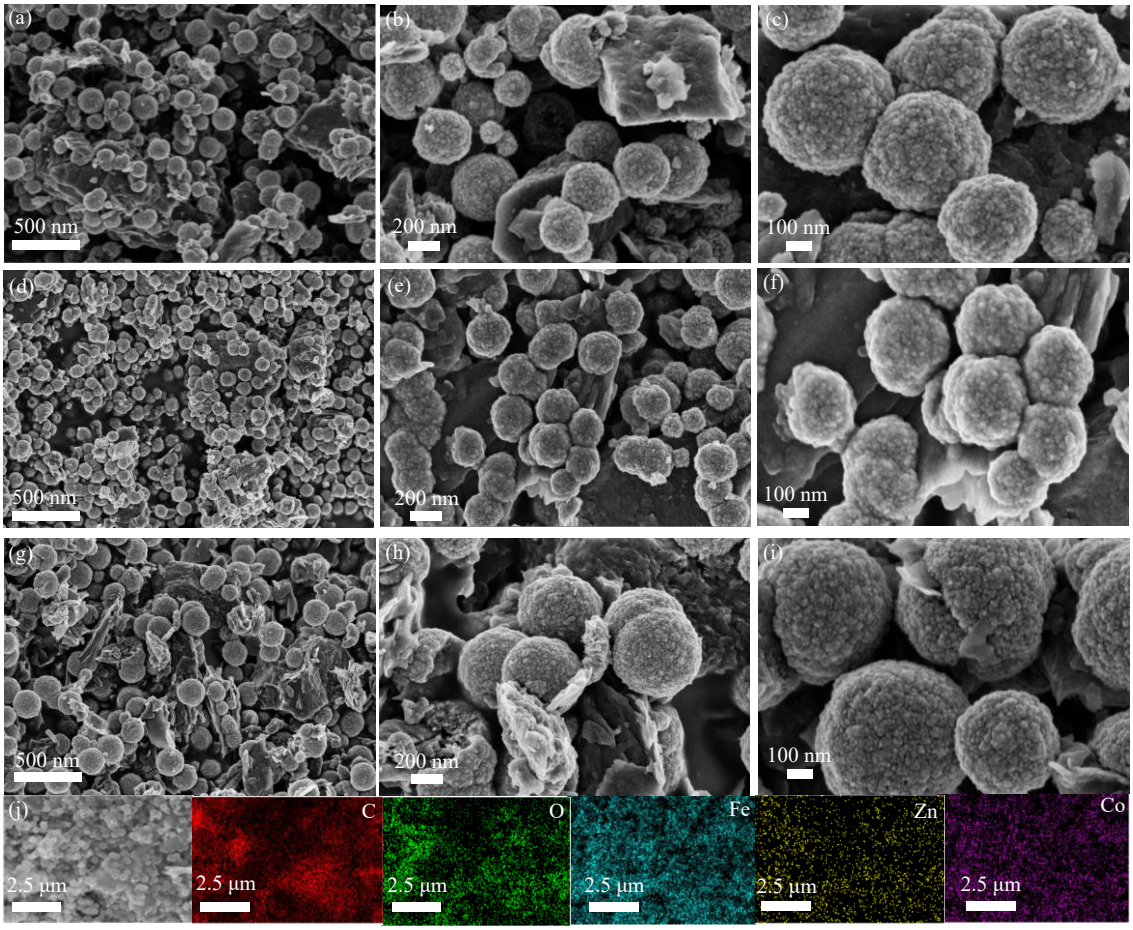

Fig. 4. SEM images of CZFO/RC composites under different resolutions: (a–c) CZFO/RC-1, (d–f) CZFO/RC-2, and (g–i) CZFO/RC-3; (j) EDS mapping of CZFO/RC-2.

larization and MA performance [69–70]. In Fig. 4(c), (f), and (i), the CZFO nanospheres loaded on RC flakes formed several heterogeneous interfaces, enhancing the interfacial polarization and promoting MA of the CZFO/RC composites. Fig. 4(j) shows the energy-dispersive X-ray spectrum (EDS) corresponding to CZFO/RC-2. The CZFO/RC composite is mainly composed of C, O, Fe, Co, and Zn elements, and the test results are consistent with the element composition of the CZFO/RC material.

The lattice spacing of 0.16 and 0.25 nm, corresponding to the (511) and (311) crystal planes of CZFO, respectively, was observed using high-resolution TEM as shown in Fig. 5(c), (f), and (i). The elemental mapping results of CZFO/RC-2 (Fig. 5(j)) are in good agreement (for all the elements) with the SEM results. These results confirm the successful synthesis of CZFO/RC composites with excellent states existing numerous polarization behavior conditions.

The XPS spectrum of CZFO/RC-2 is shown in Fig. 6. CZFO/RC-2 contains C, O, Co, Fe, and Zn elements, which is consistent with the element composition of the CZFO/RC. In Fig. 6(b), the peaks at 710.1 and 713.2 eV correspond to Fe $2p_{3/2}$, whereas that at 724.1 eV corresponds to Fe $2p_{1/2}$. In Fig. 6(c), Co $2p_{3/2}$ and Co $2p_{1/2}$ coincide with the peaks at 781.0 and 787.6 eV, respectively, indicating the presence of Co^{2+}. For high-resolution spectrum of Zn 2p orbit, the peaks at 1022.3 and 1045.4 eV can be assigned to Zn $2p_{3/2}$ and Zn $2p_{1/2}$, respectively.

3.2. Microwave absorption properties of the CZFO/RC composites

Impedance matching is necessary for the EMW to enter the absorber. Impedance matching can be calculated using Eq. (1):

$$Z_{in} = Z_0 \sqrt{\frac{\mu_r}{\varepsilon_r}} \tanh\left[j\left(\frac{2\pi f d}{c}\right) \sqrt{\mu_r \varepsilon_r} \right] \quad (1)$$

where Z_{in} is the input impedance of the CZFO/RC composite, Z_0 is the characteristic impedance of free space, μ_r and ε_r are the relative complex permittivity and complex permeability of the absorber, respectively, f, d, and c are the microwave frequency, thickness of the absorber, and speed of light, respectively.

In Fig .7, the RL, matching thickness (t_m) and impedance matching value ($|Z_{in}/Z_0|$) with absorption peak frequency (f_m) are described. According to $\lambda/4$ matching theory, the relationship between f_m and t_m can be expressed using Eq. (2).

$$t_m = \frac{n\lambda}{4} = \frac{nc}{4 f_m \sqrt{|\varepsilon_r \mu_r|}} \quad (n = 1, 3, 5, \ldots) \quad (2)$$

where λ is the wavelength.

The results show that all the t_m experimental values (t_m^{exp})

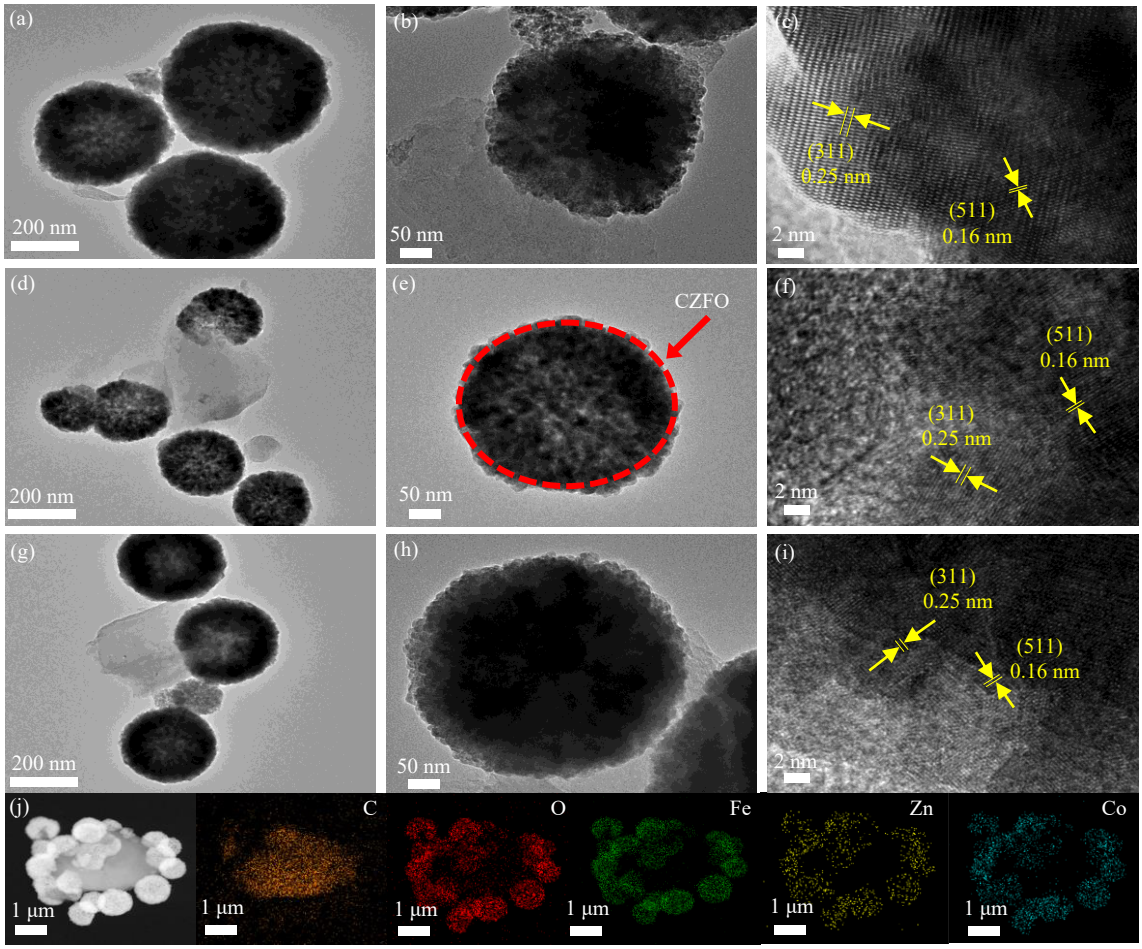

Fig. 5. TEM images of CZFO/RC composites under different resolutions: (a–c) CZFO/RC-1, (d–f) CZFO/RC-2, and (g–i) CZFO/RC-3; (j) element mapping images of CZFO/RC-2.

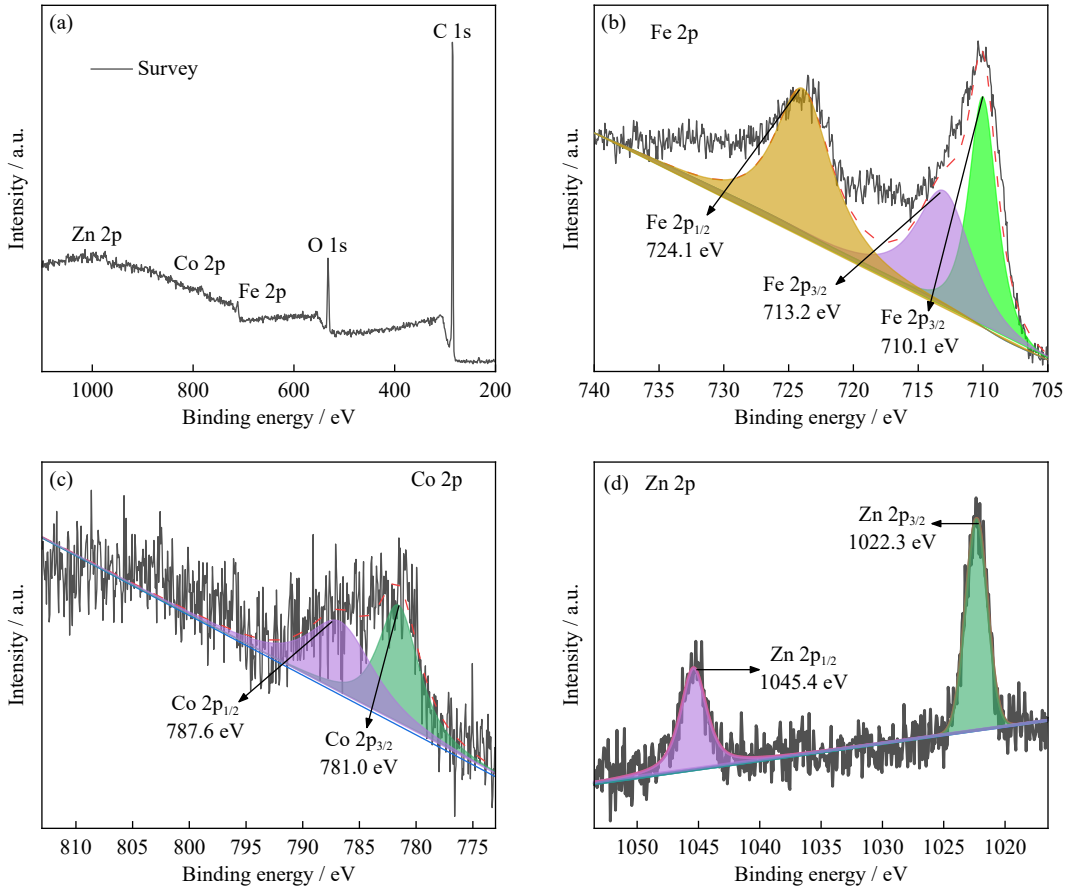

Fig. 6. XPS spectra of CZFO/RC-2 composite: (a) full spectrum, (b) Fe 2p, (c) Co 2p, and (d) Zn 2p.

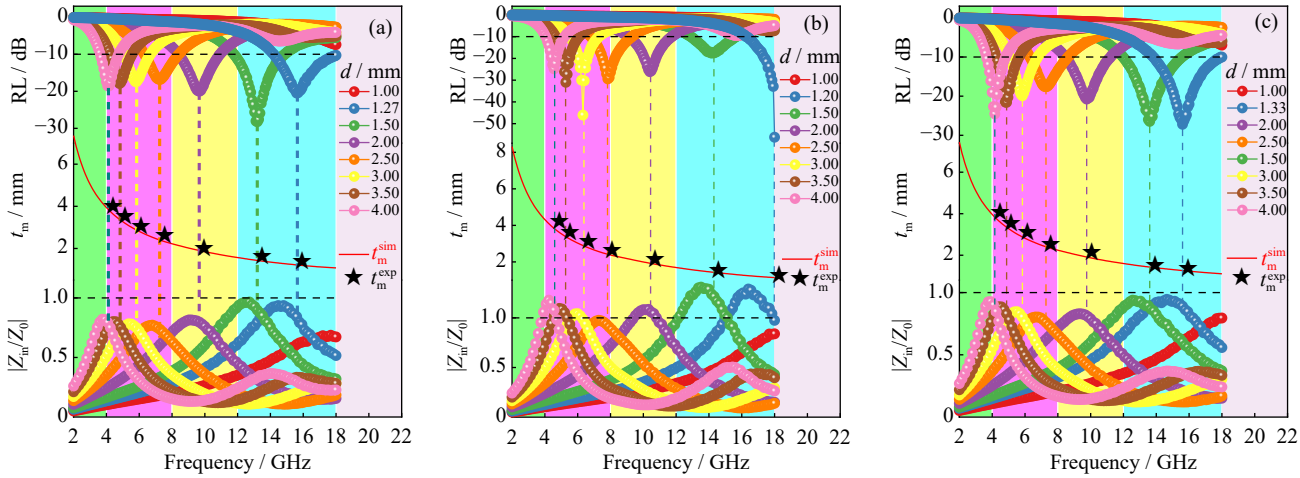

Fig. 7. RL, t_m, and $|Z_{in}/Z_0|$ vs. f_m curves of (a) CZFO/RC-1, (b) CZFO/RC-2, and (c) CZFO/RC-3.

are on the $\lambda/4$ curve (t_m^{sim} curve, the t_m simulation values), which means that the $\lambda/4$ matching theory basically dominates the relationship between f_m and t_m. When excellent MA properties are obtained, the $|Z_{in}/Z_0|$ corresponding to the frequency at which the RL_{min} is reached is almost equal to 1. The results show that the impedance matching performance of CZFO/RC-1, CZFO/RC-2, and CZFO/RC-3 are good. The excellent impedance matching of the EMW performance of CZFO/RC can be attributed to the maintenance of a good balance between complex permittivity and permeability.

The RL values of CZFO/RC composites can be calculated using Eq. (3) to evaluate their MA properties.

$$RL\,(dB) = 20\lg\left|\frac{Z_{in} - Z_0}{Z_{in} + Z_0}\right| \tag{3}$$

Fig. 8 shows the RL curve and three-dimensional (3D) diagram of the CZFO/RC composites, which are used to explore the effect of different contents of CZFO nanospheres on the absorption properties of the CZFO/RC composites. In Fig. 8(a) and (e), the RL_{min} of CZFO/RC-1 and CZFO/RC-3 are −28.31 and −27.32 dB, respectively. The EAB values are 3.08 and 4.16 GHz, respectively, indicating excellent MA performance. The RL_{min} of CZFO/RC-2 can reach −56.24 dB, and the EAB covers nearly 50% of the Ku band at a thickness of 1.20 mm. At a CZFO/RC-2 thickness of 3.00

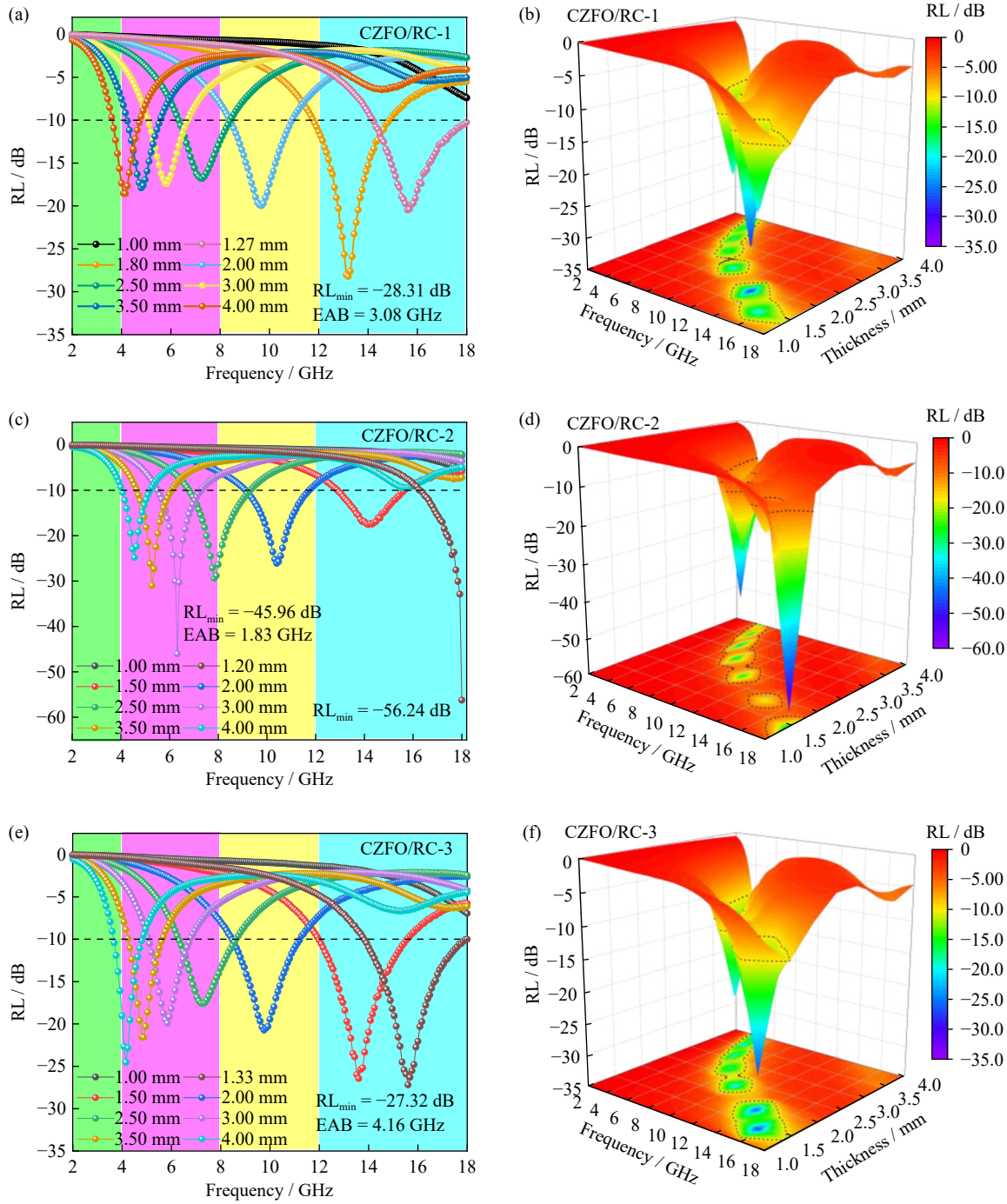

Fig. 8. RL curves and 3D plots of (a, b) CZFO/RC-1, (c, d) CZFO/RC-2, and (e, f) CZFO/RC-3 with different thicknesses.

mm, the RL_{min} is −45.96 dB at 6.34 GHz and the EAB is 1.83 GHz. Thus, the MA performance of the CZFO/RC composites can be adjusted by changing the proportion of magnetic CZFO nanospheres.

According to the MA theory, the absorption capacity of the absorber should be mainly evaluated based on the EM parameters (Fig. 9). The real part (ε', μ') of the absorber reflects its EMW storage capacity, and the imaginary part (ε'', μ'') reflects its EMW dissipation capacity. In Fig. 9(a) and (c), ε' and μ' of the CZFO/RC composites decrease with an increase in the frequency. With an increase in the CZFO nanospheres, ε' decreases, being conducive to MA attenuation, while μ' increases, improving the magnetic properties. Fig. 9(b) and (d) shows that the changes in ε'' and μ'' are complex, indicating a strong EMW dispersion effect of the absorber. CZFO/RC-1, CZFO/RC-2, and CZFO/RC-3 exhibit apparent relaxation behavior with clear polarization behavior inside the material. Fig. 9(e) and (f) shows the tangent values of the dielectric loss ($\tan\delta_\varepsilon$) and magnetic loss ($\tan\delta_\mu$) of the CZFO/RC composites, respectively. The $\tan\delta_\varepsilon$ and $\tan\delta_\mu$ are important parameters for assessing the loss capacity of absorbers, which can further clarify the loss mechanism of the composites. The results show that the $\tan\delta_\varepsilon$ value is greater than the $\tan\delta_\mu$ value, indicating that dielectric loss dominates the CZFO/RC composites.

The relationship between ε'' and ε' is expressed by Eq. (4).

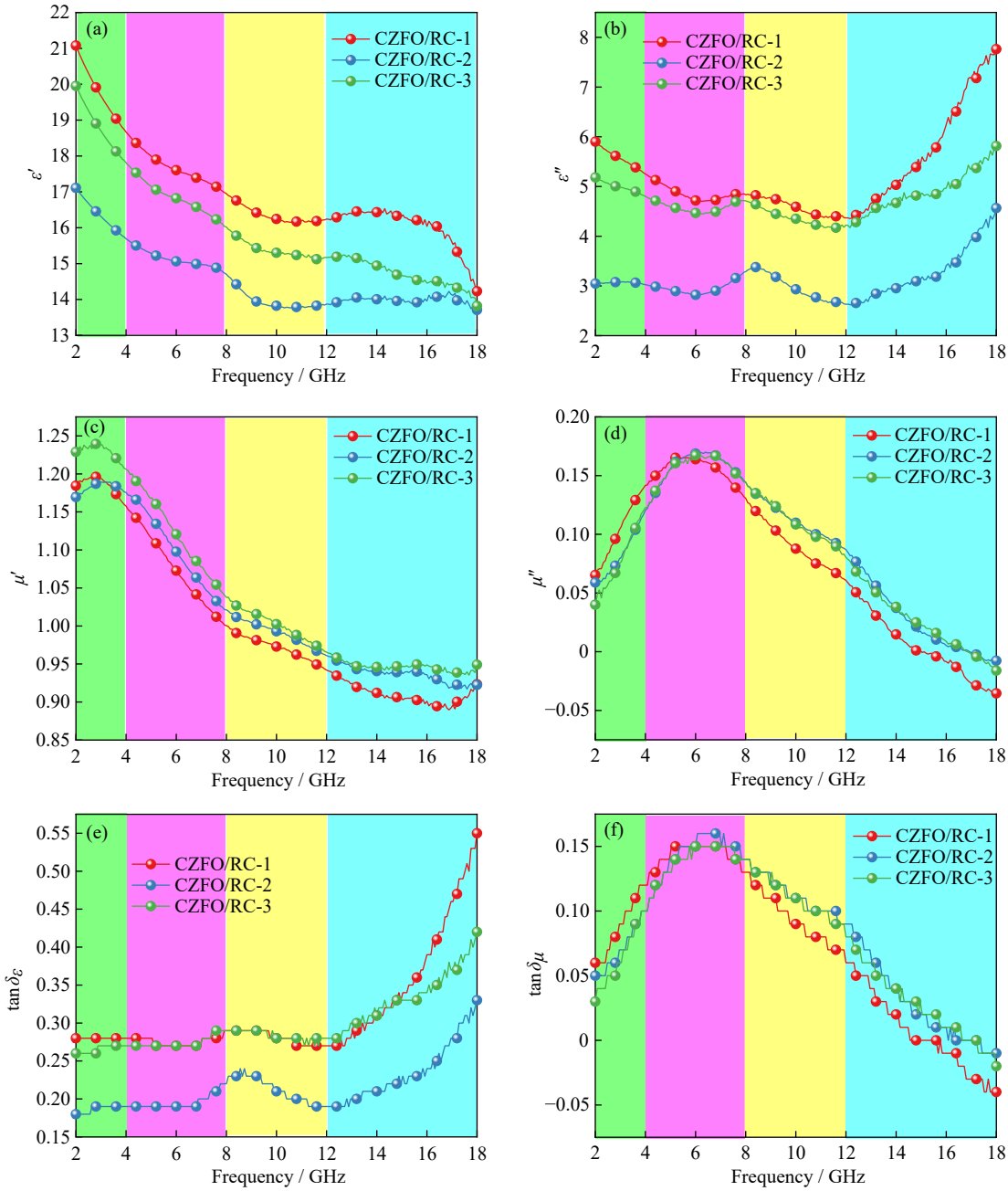

Fig. 9. Electromagnetic parameters of CZFO/RC composites: (a) ε', (b) ε'', (c) μ', (d) μ'', (e) $\tan\delta_\varepsilon$, and (f) $\tan\delta_\mu$.

$$\left(\varepsilon' - \frac{\varepsilon_s + \varepsilon_\infty}{2}\right)^2 + (\varepsilon'')^2 = \left(\frac{\varepsilon_s - \varepsilon_\infty}{2}\right)^2 \quad (4)$$

where ε_s is the static dielectric constant and ε_∞ is the relative dielectric constant of the composites.

During Debye relaxation, the curve of the ε'' vs. ε' of the EMW absorber should be a Cole–Cole semicircle. Each semicircle denotes a Debye relaxation process that enhances the MA capability of the absorber [71]. In Fig. 10(a)–(c), the CZFO/RC composites exhibit two Cole–Cole semicircles, indicating that part of the dielectric loss of the CZFO/RC composite is attributed to interfacial polarization. According to relevant studies, natural resonance and eddy current losses are the main reasons of magnetic loss in magnetodielectric composites [72–74]. Eq. (5) shows that the eddy current loss is affected by the diameter (D) and conductivity (σ). Magnetic loss is caused only by eddy current loss at a constant C_0. In Fig. 10(d), the fluctuation of C_0 suggests that the magnetic loss is not only caused by eddy current loss, but also by other forms of loss mechanisms.

$$\mu'' \approx \frac{2\pi\mu_0(\mu')^2\sigma D^2 f}{3} \quad (5)$$

$$C_0 = \mu''(\mu')^{-2} f^{-1} \quad (6)$$

where μ_0 is the permeability of vacuum.

The attenuation constant (α) is often used to reflect the EMW attenuation capacity of absorbers:

$$\alpha = \frac{\sqrt{2}\pi f}{c} \times \sqrt{(\mu''\varepsilon'' - \mu'\varepsilon') + \sqrt{(\mu''\varepsilon'' - \mu'\varepsilon')^2 + (\varepsilon'\mu'' + \varepsilon''\mu')^2}} \quad (7)$$

Fig. 10(e) shows that among the three samples, CZFO/

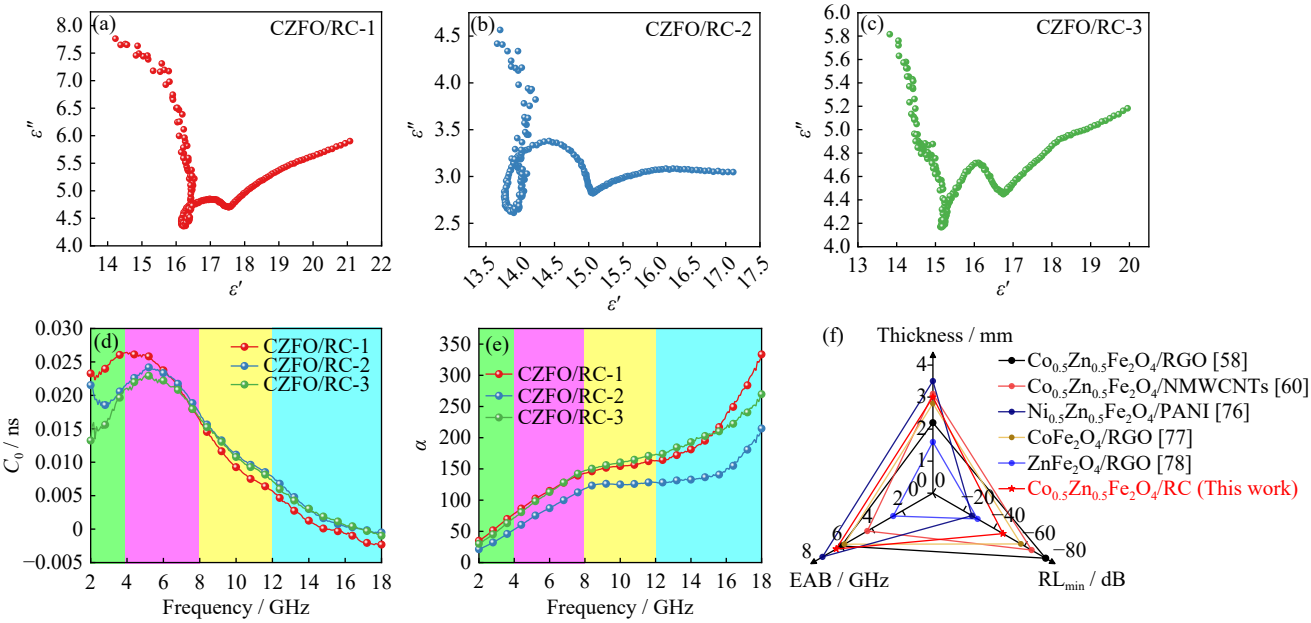

Fig. 10. (a–c) Cole–Cole curves, (d) C_0, and (e) α of CZFO/RC composites; (f) MA performance of some magnetic carbon-based composites.

RC-2 has the lowest α value, whereas CZFO/RC-2 exhibits the best MA performance. This is in good agreement with the above results.

The excellent MA performance of CZFO/RC are mainly due to the following reasons (Fig. 11). First, RC has a suitable dielectric constant, providing an absorber with a suitable impedance match. Second, the presence of numerous defects and a wide range of oxygen-containing functional groups (e.g., –COOH) can generate defects and dipole polarizations at the RC interface, reducing the EMW energy [75]. Third, numerous CZFO nanospheres get adsorbed on the RC interface, generating a heterogeneous interface between the CZFO nanospheres and RC. This heterogeneous surface can attenuate the energy of the incident EMW through polar bonds or electric charge. Fourth, the EM energy is absorbed by electrons, allowing them to migrate and jump between the carbon layers of RC. According to Cao's electron jump theory, the absorbance of EM energy by electrons promotes its conversion into thermal energy. Finally, the CZFO nanospheres introduce natural resonance and eddy currents into the composite, further attenuating the incident EMWs. Moreover, the magnetic of CZFO nanospheres can cause magnetic loss, thereby enhancing the loss mechanism. Therefore, compared with magnetic carbon-matrix composites, which exhibit a magnetodielectric cooperative loss mechanism [58,60,76–78], CZFO/RC composites excellent efficient MA properties (Fig. 10(f)).

Stealth aircraft use RCS to measure radar wave scattering capability. A perfect conductor substrate (PEC, 180 mm × 180 mm, d = 1.0 mm, f = 18.00 GHz) coated with the CZFO/RC composites was simulated using commercial EM field simulation software. Fig. 12 shows the 3D intensity images and RCS curves of the PEC and PEC coated with CZFO/RC-2 at −90°–90°. At 18.00 GHz, the maximum RCS value of

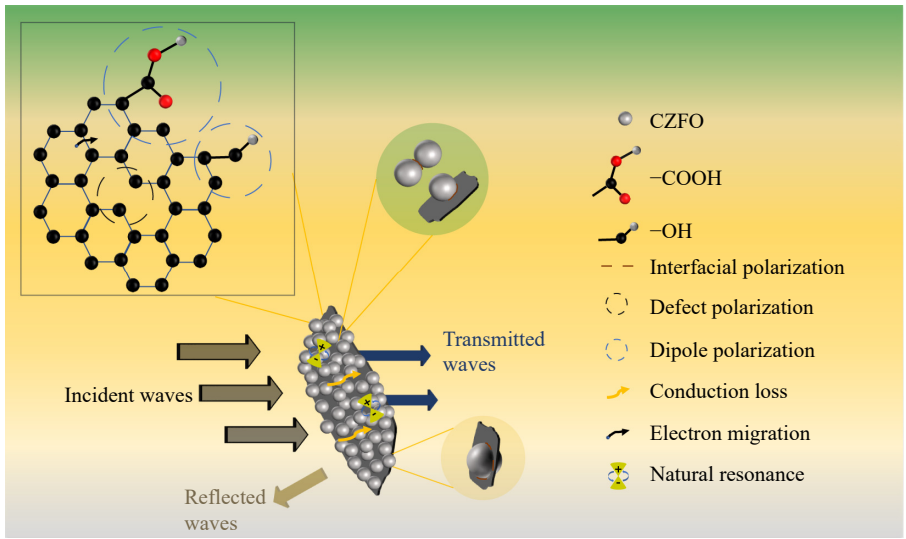

Fig. 11. MA mechanisms of CZFO/RC composites.

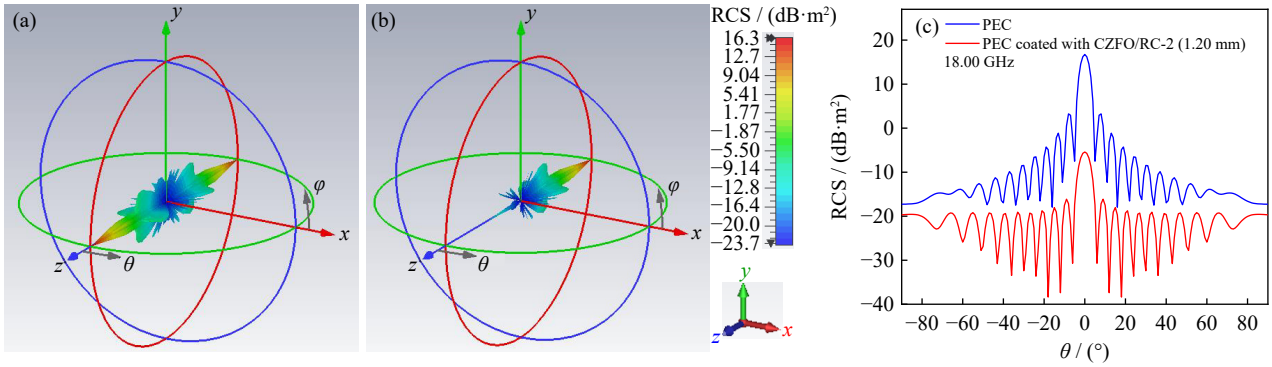

Fig. 12. RCS simulation plots results: 3D intensity images of (a) PEC model and (b) PEC coated with CZFO/RC-2; (c) RCS curve of PEC and CZFO/RC-2 (1.20 mm) coated PEC at 18.00 GHz.

CZFO/RC-2 coated PEC (1.20 mm) is considerably smaller than that of the pure PEC model, indicating that the CZFO/RC-2 coating can lower the radar scattering intensity of the PEC model. The RCS simulation results confirm that the CZFO/RC composites exhibit excellent RCS reduction ability and can effectively decrease the EM scattering of the PEC substrates.

4. Conclusion

CZFO/RC composites were successfully produced via a hydrothermal method, in which CZFO nanospheres were uniformly distributed on the RC. CZFO/RC-2 exhibits excellent MA performance (RL_{min} = −56.24 dB and thickness = 1.20 mm). Even at 6.34 GHz and a CZFO/RC-2 thickness of 3.00 mm, RL_{min} reaches −45.96 dB with a maximum EAB of 1.83 GHz (5.53–7.36 GHz). Interfacial and dipole polarizations are the main sources of dielectric loss in CZFO nanospheres. The results show that the CZFO/RC composites exhibit a special heterostructure, good impedance matching, and various EM loss mechanisms, indicating their excellent MA performance. This study expands the application of CGFS in the field of microwave absorption.

Acknowledgements

This work was financially supported by the National Natural Science Foundation of China (No. 52200139), the Open Research Grant of Joint National-Local Engineering Research Centre for Safe and Precise Coal Mining, China (No. EC2023013), and the Scientific Research Foundation for the Introduction of Talent in Anhui University of Science and Technology, China (No. 2023yjrc79).

Conflict of Interest

The authors declare that there is no conflict of financial or non-financial interests.

References

[1] D. Raphaeli and I. Bilik, Challenges in automotive MIMO radar calibration in anechoic chamber, *IEEE Trans. Aerosp. Electron. Syst.*, 59(2023), No. 5, p. 6205.

[2] K. Cha, S. Oh, H. Hong, H. Park, and S.K. Hong, Detection of electronic devices using FMCW nonlinear radar, *Sensors*, 22(2022), No. 16, art. No. 6086.

[3] Y.H. Liu, Y. Shen, L.L. Fan, *et al.*, Parallel radars: From digital twins to digital intelligence for smart radar systems, *Sensors*, 22(2022), No. 24, art. No. 9930.

[4] J. Reimann, A.M. Büchner, S. Raab, K. Weidenhaupt, M. Jirousek, and M. Schwerdt, Highly accurate radar cross-section and transfer function measurement of a digital calibration transponder without known reference—Part I: Measurement and results, *Remote. Sens.*, 15(2023), No. 4, art. No. 1153.

[5] L.Y. Xiao, Y.J. Xie, S.D. Gao, J.B. Li, and P.Y. Wu, Generalized radar range equation applied to the whole field region, *Sensors*, 22(2022), No. 12, art. No. 4608.

[6] H. Bang, Y.S. Yan, A. Basit, W.Q. Wang, and J. Cheng, Radar cross section characterization of frequency diverse array radar, *IEEE Trans. Aerosp. Electron. Syst.*, 59(2023), No. 1, p. 460.

[7] S. Björklund and H. Hernnäs, Statistical analysis of the radar cross section of two small fixed-wing drones using typical flights, *IET Radar Sonar Navig.*, 18(2024), No. 1, p. 125.

[8] D. Bacci and I. Vagias, A trade-off analysis between lateral/directional stability and radar cross section requirements of an air-to-air combat airframe, *Aerosp. Sci. Technol.*, 138(2023), art. No. 108361.

[9] Y.Y. He, X.W. Wu, G.B. Hu, and W.D. Ke, A new way to achieve infrared stealth by composite phase change microcapsules, *J. Energy Storage*, 73(2023), art. No. 109217.

[10] M. Han, D. Zhang, C.E. Shuck, *et al.*, Electrochemically modulated interaction of MXenes with microwaves, *Nat. Nanotechnol.*, 18(2023), No. 4, p. 373.

[11] X. Yang, L.X. Xuan, W.W. Men, *et al.*, Carbonyl iron/glass fiber cloth composites: Achieving multi-spectrum stealth in a wide temperature range, *Chem. Eng. J.*, 491(2024), art. No. 151862.

[12] W. Li, Z.J. Yu, Q.B. Wen, *et al.*, Ceramic-based electromagnetic wave absorbing materials and concepts towards lightweight, flexibility and thermal resistance, *Int. Mater. Rev.*, 68(2023), No. 5, p. 487.

[13] B. Dai, Y. Ma, F. Dong, *et al.*, Overview of MXene and conducting polymer matrix composites for electromagnetic wave absorption, *Adv. Compos. Hybrid Mater.*, 5(2022), No. 2, p. 704.

[14] G.W. Ma, J.B. Sun, F. Aslani, Y.M. Huang, and F.Y. Jiao, Review on electromagnetic wave absorbing capacity improvement of cementitious material, *Constr. Build. Mater.*, 262(2020), art. No. 120907.

[15] Y. Li, Y.C. Qing, Y.R. Zhang, and H.L. Xu, Simultaneously tuning structural defects and crystal phase in accordion-like Ti_xO_{2x-1} derived from $Ti_3C_2T_x$ MXene for enhanced electromagnetic attenuation, *J. Adv. Ceram.*, 12(2023), No. 10, p. 1946.

[16] R.Z. Zhao, T. Gao, Y.X. Li, *et al*., Highly anisotropic Fe_3C microflakes constructed by solid-state phase transformation for efficient microwave absorption, *Nat. Commun.*, 15(2024), No. 1, art. No. 1497.
[17] Z.M. Tang, L. Xu, C. Xie, *et al*., Synthesis of $CuCo_2S_4$@expanded graphite with crystal/amorphous heterointerface and defects for electromagnetic wave absorption, *Nat. Commun.*, 14(2023), No. 1, art. No. 5951.
[18] F. Shahzad, M. Alhabeb, C.B. Hatter, *et al*., Electromagnetic interference shielding with 2D transition metal carbides (MXenes), *Science*, 353(2016), No. 6304, p. 1137.
[19] J.J. Li, D. Lan, Y.H. Cheng, *et al*., Constructing mixed-dimensional lightweight magnetic cobalt-based composites heterostructures: An effective strategy to achieve boosted microwave absorption and self-anticorrosion, *J. Mater. Sci. Technol.*, 196(2024), p. 60.
[20] S. Anand and P. Prashalee, Wide axial ratio bandwidth dual polarized S, C, X, and Ku band antenna using orthogonal SIW, *Wirel. Pers. Commun.*, 122(2022), No. 3, p. 2885.
[21] D. Lan, Y. Hu, M. Wang, Y. Wang, Z.G. Gao, and Z.R. Jia, Perspective of electromagnetic wave absorbing materials with continuously tunable effective absorption frequency bands, *Compos. Commun.*, 50(2024), art. No. 101993.
[22] N. Kanellos, D. Katsianis, and D. Varoutas, Assessing the impact of emerging vertical markets on 5G diffusion forecasting, *IEEE Commun. Mag.*, 61(2023), No. 2, p. 38.
[23] P. Vargas and I. Tien, Methodology to quantitatively assess impacts of 5G telecommunications cybersecurity risk scenarios on dependent connected urban transportation systems, *ASCE-ASME J. Risk Uncertainty Eng. Syst. Part A*, 8(2022), No. 2, art. No. 04022004.
[24] H. Hinrikus, T. Koppel, J. Lass, H. Orru, P. Roosipuu, and M. Bachmann, Possible health effects on the human brain by various generations of mobile telecommunication: A review based estimation of 5G impact, *Int. J. Radiat. Biol.*, 98(2022), No. 7, p. 1210.
[25] G. Singh, R. Casson, and W. Chan, The potential impact of 5G telecommunication technology on ophthalmology, *Eye*, 35(2021), No. 7, p. 1859.
[26] C. Jiang and B.Y. Wen, Construction of 1D heterogeneous Co/C@Ag nws with tunable electromagnetic wave absorption and shielding performance, *Small*, 19(2023), No. 34, art. No. e2301760.
[27] K. Suslov, A. Kryukov, P. Ilyushin, A. Cherepanov, and A. Kryukov, Modeling the effects of electromagnetic interference from multi-wire traction networks on pipelines, *Energies*, 16(2023), No. 10, art. No. 4188.
[28] N.N. Wu, B.B. Zhao, Y.Y. Lian, *et al*., Metal organic frameworks derived Ni_xSe_y@NC hollow microspheres with modifiable composition and broadband microwave attenuation, *Carbon*, 226(2024), art. No. 119215.
[29] Z.G. Gao, D. Lan, X.Y. Ren, Z.R. Jia, and G.L. Wu, Manipulating cellulose-based dual-network coordination for enhanced electromagnetic wave absorption in magnetic porous carbon nanocomposites, *Compos. Commun.*, 48(2024), art. No. 101922.
[30] Q.L. Zhang, D. Lan, S.L. Deng, *et al*., Constructing multiple heterogeneous interfaces in one-dimensional carbon fiber materials for superior electromagnetic wave absorption, *Carbon*, 226(2024), art. No. 119233.
[31] J.X. Zhou, X.M. Huang, D. Lan, *et al*., Polymorphic cerium-based Prussian blue derivatives with *in situ* growing CNT/Co heterojunctions for enhanced microwave absorption via polarization and magnetization, *Nano Res.*, 17(2024), No. 3, p. 2050.
[32] Y. Shen, G.H. Lu, Y.H. Bai, *et al*., Structural features of residue carbon formed by gasification of different coal macerals, *Fuel*, 320(2022), art. No. 123918.
[33] R. Han, A.N. Zhou, N.N. Zhang, *et al*., Structural properties of residual carbon in coal gasification fine slag and their influence on flotation separation and resource utilization: A review, *Int. J. Miner. Metall. Mater.*, 31(2024), art. No. 2, p. 217.
[34] X.T. Fan, P.P. Fan, Z.Y. Ren, *et al*., Separation and physicochemical properties of residual carbon in gasification slag, *Physicochem. Probl. Miner. Process.*, 58(2022), No. 6, art. No. 154928.
[35] P. Lv, B. Liu, Y.H. Bai, *et al*., Residual carbon from coal gasification fine slag for inducing rice straw hydrothermal carbonization to achieve improved reactivity and wastewater decontamination, *Fuel*, 349(2023), art. No. 128649.
[36] L.R. Mao, M.D. Zheng, B.L. Xia, *et al*., Effect of residual carbon on coal ash melting characteristics in reducing atmosphere, *Fuel*, 346(2023), art. No. 128385.
[37] G.M. Li, X.J. Xue, L.T. Mao, *et al*., Recycling and utilization of coal gasification residues for fabricating Fe/C composites as novel microwave absorbents, *Int. J. Miner. Metall. Mater.*, 30(2023), art. No. 3, p. 591.
[38] F.H. Guo, X. Zhao, Y. Guo, Y.X. Zhang, and J.J. Wu, Fractal analysis and pore structure of gasification fine slag and its flotation residual carbon, *Colloids Surf. A*, 585(2020), art. No. 124148.
[39] Y.C. Zhang, S.T. Gao, J. He, H.X. Li, C.L. Wu, and Y.H. Bai, PANI-wrapped high-graphitized residual carbon hybrid with boosted electromagnetic wave absorption performance, *Synth. Met.*, 287(2022), art. No. 117077.
[40] K. Li, Q.F. Liu, H.F. Cheng, M.S. Hu, and S. Zhang, Classification and carbon structural transformation from anthracite to natural coaly graphite by XRD, Raman spectroscopy, and HRTEM, *Spectrochim. Acta Part A*, 249(2021), art. No. 119286.
[41] B. Lv, X.W. Deng, F.S. Jiao, B.B. Dong, C.J. Fang, and B.L. Xing, Enrichment and utilization of residual carbon from coal gasification slag: A review, *Process. Saf. Environ. Prot.*, 171(2023), p. 859.
[42] Q.Y. Wang, Y.H. Bai, P. Lv, *et al*., Separation and characterization of different types of residual carbon in fine slag from entrained flow coal gasification, *Fuel*, 339(2023), art. No. 127437.
[43] S.T. Gao, Y.C. Zhang, H.X. Li, J. He, H. Xu, and C.L. Wu, The microwave absorption properties of residual carbon from coal gasification fine slag, *Fuel*, 290(2021), art. No. 120050.
[44] M. Kaur and S. Bahel, Characterization of sol–gel synthesized $Zn_{0.25}Co_{0.75}(NiZr)_xFe_{2-2x}O_4$ ($0.05 \le x \le 0.25$) spinel ferrites based microwave absorbers in Ka frequency band, *J. Phys. Chem. Solids*, 184(2024), art. No. 111671.
[45] M. Kaur and S. Bahel, Fabrication of $Zn_{0.25}Co_{0.75}(MnZr)_xFe_{2-2x}O_4$ spinel ferrites as broadband microwave absorbers in 26.5–40 GHz frequency range, *J. Alloys Compd.*, 954(2023), art. No. 170154.
[46] F. Hosseini Mohammadabadi, S.M. Masoudpanah, S. Alamolhoda, and H.R. Koohdar, High-performance microwave absorbers based on $(CoNiCuZn)_{1-x}Mn_xFe_2O_4$ spinel ferrites, *J. Alloys Compd.*, 909(2022), art. No. 164637.
[47] R.S. Yadav, Anju, and I. Kuřitka, Spinel ferrite and MXene-based magnetic novel nanocomposites: An innovative high-performance electromagnetic interference shielding and microwave absorber, *Crit. Rev. Solid State Mater. Sci.*, 48(2023), No. 4, p. 441.
[48] X.L. Chen, D. Lan, L.T. Zhou, *et al*., Rational construction of $ZnFe_2O_4$ decorated hollow carbon cloth towards effective electromagnetic wave absorption, *Ceram. Int.*, 50(2024), No. 13, p. 24549.
[49] B. Shi, H.S. Liang, and Z.J. Xie, *et al*., Dielectric loss enhancement induced by the microstructure of $CoFe_2O_4$ foam to realize broadband electromagnetic wave absorption, *Int. J. Miner. Metall. Mater.*, 30(2023), art. No. 7, p. 1388.
[50] G.J. Ma, D. Lan, Y. Zhang, *et al*., Microporous cobalt ferrite with bio-carbon loosely decorated to construct multi-functional

composite for dye adsorption, anti-bacteria and electromagnetic protection, *Small*, 20(2024), No. 45, art. No. e2404449.
[51] A. Houbi, Z.A. Aldashevich, Y. Atassi, Z. Bagasharova Telmanovna, M. Saule, and K. Kubanych, Microwave absorbing properties of ferrites and their composites: A review, *J. Magn. Magn. Mater.*, 529(2021), art. No. 167839.
[52] M. Derakhshani, E. Taheri-Nassaj, M. Jazirehpour, and S.M. Masoudpanah, Structural, magnetic, and gigahertz-range electromagnetic wave absorption properties of bulk Ni–Zn ferrite, *Sci. Rep.*, 11(2021), No. 1, art. No. 9468.
[53] X.B. Xie, B.L. Wang, Y.K. Wang, C. Ni, X.Q. Sun, and W. Du, Spinel structured MFe_2O_4 (M = Fe, Co, Ni, Mn, Zn) and their composites for microwave absorption: A review, *Chem. Eng. J.*, 428(2022), art. No. 131160.
[54] Y. Mu, Z.H. Ma, H.S. Liang, L.M. Zhang, and H.J. Wu, Ferrite-based composites and morphology-controlled absorbers, *Rare Met.*, 41(2022), No. 9, p. 2943.
[55] Y. Han, D. Lan, M.J. Han, Z.H. Xia, J.X. Zou, and Z.R. Jia, Construction of flower-like MoS_2 decorated on Cu doped CoZn-ZIF derived N-doped carbon as superior microwave absorber, *Nano Res.*, 17(2024), No. 9, p. 8250.
[56] J. Yan, Z.D. Ye, D. Lan, W.X. Chen, Z.R. Jia, and G.L. Wu, Transition metal carbides towards electromagnetic wave absorption application: State of the art and perspectives, *Compos. Commun.*, 48(2024), art. No. 101954.
[57] Y.W. Liu, J. Zhang, L.S. Gu, L.X. Wang, and Q.T. Zhang, Preparation and electromagnetic properties of nanosized $Co_{0.5}Zn_{0.5}Fe_2O_4$ ferrite, *Rare Met.*, 41(2022), No. 9, p. 3228.
[58] J.B. Zhang, R.W. Shu, Y. Wu, Z.L. Wan, and X.H. Li, Facile synthesis of $Co_{0.5}Zn_{0.5}Fe_2O_4$ nanoparticles decorated reduced graphene oxide hybrid nanocomposites with enhanced electromagnetic wave absorption properties, *Ceram. Int.*, 46(2020), No. 10, p. 15925.
[59] Z.J. Ma, C.Y. Mang, H.T. Zhao, Z.H. Guan, and L. Cheng, Comparison of electromagnetism behavior of different content cobalt–zinc ferrite loaded with graphene, *J. Inorg. Mater.*, 34(2019), No. 4, art. No. 407.
[60] R.W. Shu, Y. Wu, Z.Y. Li, *et al.*, Facile synthesis of cobalt–zinc ferrite microspheres decorated nitrogen-doped multi-walled carbon nanotubes hybrid composites with excellent microwave absorption in the X-band, *Compos. Sci. Technol.*, 184(2019), art. No. 107839.
[61] Y.Y. Lian, D. Lan, X.D. Jiang, *et al.*, Multifunctional electromagnetic wave absorbing carbon fiber/$Ti_3C_2T_X$ MXene fabric with superior near-infrared laser dependent photothermal antibacterial behaviors, *J. Colloid Interface Sci.*, 676(2024), p. 217.
[62] X.G. Su, Y. Zhang, J. Wang, and Y.Q. Liu, Enhanced electromagnetic wave absorption and mechanical performances of graphite nanosheet/PVDF foams via ice dissolution and normal pressure drying, *J. Mater. Chem. C*, 12(2024), No. 21, p. 7775.
[63] D.L. Tan, Q. Wang, M.R. Li, *et al.*, Magnetic media synergistic carbon fiber@Ni/NiO composites for high-efficiency electromagnetic wave absorption, *Chem. Eng. J.*, 492(2024), art. No. 152245.
[64] M.T. Qiao, Y.R. Tian, J.N. Wang, *et al.*, Magnetic-field-induced vapor-phase polymerization to achieve PEDOT-decorated porous Fe_3O_4 particles as excellent microwave absorbers, *Ind. Eng. Chem. Res.*, 61(2022), No. 35, p. 13072.
[65] Y.C. Zhang, S.T. Gao, J. He, F. Wei, and X.Z. Zhang, CoFe@C composites decorated with residual carbon as an ultrathin microwave absorber in the X and Ku bands, *Diam. Relat. Mater.*, 141(2024), art. No. 110666.
[66] S.T. Gao, Y.C. Zhang, J. He, *et al.*, Coal gasification fine slag residual carbon decorated with hollow-spherical Fe_3O_4 nanoparticles for microwave absorption, *Ceram. Int.*, 49(2023), No. 11, p. 17554.
[67] Y.C. Zhang, H.X. Li, S.T. Gao, Y. Geng, and C.L. Wu, A study on the chemical state of carbon present in fine ash from gasification, *Asia Pac. J. Chem. Eng.*, 14(2019), No. 4, art. No. e2336.
[68] J.L. Zhang, H.J. Yang, G.X. Shen, P. Cheng, J.Y. Zhang, and S.W. Guo, Reduction of graphene oxide via L-ascorbic acid, *Chem. Commun.*, 46(2010), No. 7, p. 1112.
[69] Z.R. Jia, J.K. Liu, Z.G. Gao, C.H. Zhang, and G.L. Wu, Molecular intercalation-induced two-phase evolution engineering of 1T and 2H-MS_2 (M = Mo, V, W) for interface-polarization-enhanced electromagnetic absorbers, *Adv. Funct. Mater.*, (2024), art. No. 2405523.
[70] Y.F. He, Q. Su, D.D. Liu, *et al.*, Surface engineering strategy for MXene to tailor electromagnetic wave absorption performance, *Chem. Eng. J.*, 491(2024), art. No. 152041.
[71] H.L. Lv, Y.H. Guo, G.L. Wu, G.B. Ji, Y. Zhao, and Z.J. Xu, Interface polarization strategy to solve electromagnetic wave interference issue, *ACS Appl. Mater. Interfaces*, 9(2017), No. 6, p. 5660.
[72] W.Q. Guo, B. Hong, J.C. Xu, *et al.*, CNTs-improved electromagnetic wave absorption performance of Sr-doped Fe_3O_4/CNTs nanocomposites and physical mechanism, *Diam. Relat. Mater.*, 141(2024), art. No. 110699.
[73] Y.H. Bai, D.Y. Zhang, and Y. Lu, Foamed concrete composites: Mn–Zn ferrite/carbon fiber synergy enhances electromagnetic wave absorption performance, *Ceram. Int.*, 49(2023), No. 21, p. 33703.
[74] S.F. Zeng, M.Y. Wang, W.L. Feng, *et al.*, Cobalt nanoparticles encapsulated in a nitrogen and oxygen dual-doped carbon matrix as high-performance microwave absorbers, *Inorg. Chem. Front.*, 6(2019), No. 9, p. 2472.
[75] X.G. Su, J. Wang, T. Liu, *et al.*, Controllable atomic migration in microstructures and defects for electromagnetic wave absorption enhancement, *Adv. Funct. Mater.*, 34(2024), No. 9, art. No. 2403397.
[76] X.F. Meng, Q.X. Han, Y.J. Sun, and Y.F. Liu, Synthesis and microwave absorption properties of $Ni_{0.5}Zn_{0.5}Fe_2O_4$/$BaFe_{12}O_{19}$@polyaniline composite, *Ceram. Int.*, 45(2019), No. 2, p. 2504.
[77] Y. Liu, Z. Chen, Y. Zhang, *et al.*, Broadband and lightweight microwave absorber constructed by *in situ* growth of hierarchical $CoFe_2O_4$/reduced graphene oxide porous nanocomposites, *ACS Appl. Mater. Interfaces*, 10(2018), No. 16, p. 13860.
[78] Z.W. Yang, Y.Z. Wan, G.Y. Xiong, *et al.*, Facile synthesis of $ZnFe_2O_4$/reduced graphene oxide nanohybrids for enhanced microwave absorption properties, *Mater. Res. Bull.*, 61(2015), p. 292.